

1 Search for the double-beta decay of ^{82}Se to the excited states
2 of ^{82}Kr with NEMO-3

3 R. Arnold^a, C. Augier^b, A.S. Barabash^c, A. Basharina-Freshville^d, S. Blondel^b, S. Blot^e,
4 M. Bongrand^b, D. Boursette^b, R. Breier^t, V. Brudanin^{f,g}, J. Busto^h, A.J. Caffreyⁱ, S.
5 Calvez^b, M. Cascella^b, C. Cerna^j, J. P. Cesar^k, A. Chapon^l, E. Chauveau^j, A. Chopra^d,
6 L. Dawson^d, D. Duchesneau^m, D. Durand^l, V. Egorov^{f,1}, G. Eurin^{b,d}, J.J. Evans^e,
7 L. Fajtⁿ, D. Filosofov^f, R. Flack^d, X. Garrido^b, C. Girard-Carillo^b, H. Gómez^b,
8 B. Guillon^l, P. Guzowski^e, R. Hodákⁿ, A. Huber^j, P. Hubert^j, C. Hugon^j, S. Jullian^b,
9 A. Klimenko^f, O. Kochetov^f, S.I. Konovalov^c, V. Kovalenko^f, D. Lalanne^b, K. Lang^k,
10 Y. Lemièr^e, T. Le Noblet^m, Z. Liptak^k, X. R. Liu^d, P. Loaiza^b, G. Lutter^j, M. Mackoⁿ,
11 C. Macolino^b, F. Mamedovⁿ, C. Marquet^j, F. Mauger^l, A. Minotti^m, B. Morgan^o,
12 J. Mott^{d,p}, I. Nemchenok^f, M. Nomachi^q, F. Nova^k, F. Nowacki^a, H. Ohsumi^f,
13 G. Oliviero^l, R.B. Pahlka^k, V. Palusova^{j,t}, C. Patrick^d, F. Perrot^{j,*}, A. Pin^j,
14 F. Piquemal^{j,s}, P. Povinec^t, P. Přidalⁿ, Y.A. Ramachers^o, A. Remoto^m, J.L. Reyss^u,
15 B. Richards^d, C.L. Riddleⁱ, E. Rukhadzeⁿ, R. Saakyan^d, R. Salazar^k, X. Sarazin^b,
16 J. Sedgbeer^v, Yu. Shitov^f, L. Simard^{b,w}, F. Šimkovic^t, A. Smetanaⁿ, K. Smolekⁿ,
17 A. Smolnikov^f, S. Söldner-Rembold^e, B. Soulé^{j,*}, I. Šteklⁿ, J. Suhonen^x, C.S. Sutton^y,
18 G. Szklarz^b, H. Tedjiti^h, J. Thomas^d, V. Timkin^f, S. Torre^d, V.I. Tretyak^z,
19 V.I. Tretyak^f, V.I. Umatov^c, I. Vanushin^c, C. Vilela^d, V. Vorobel^{aa}, D. Waters^d,
20 F. Xie^d, A. Žukauskas^{aa}, The NEMO-3 collaboration

21 ^aIPHC, ULP, CNRS/IN2P3, F-67037 Strasbourg, France

22 ^bLAL, Univ Paris-Sud, CNRS/IN2P3, F-91405 Orsay, France

23 ^cNRC "Kurchatov Institute" - ITEP, 117218 Moscow, Russia

24 ^dUCL, London WC1E 6BT, United Kingdom

25 ^eUniversity of Manchester, Manchester M13 9PL, United Kingdom

26 ^fJINR, 141980 Dubna, Russia

27 ^gNational Research Nuclear University MEPhI, 115409 Moscow, Russia

28 ^hAix Marseille Univ., CNRS, CPPM, Marseille, France

29 ⁱIdaho National Laboratory, Idaho Falls, ID 83415, U.S.A.

30 ^jCENBG, Université de Bordeaux, CNRS/IN2P3, F-33175 Gradignan, France

31 ^kUniversity of Texas at Austin, Austin, TX 78712, U.S.A.

32 ^lLPC Caen, ENSICAEN, Université de Caen, CNRS/IN2P3, F-14050 Caen, France

33 ^mLAPP, Université de Savoie, CNRS/IN2P3, F-74941 Annecy-le-Vieux, France

34 ⁿInstitute of Experimental and Applied Physics, Czech Technical University in Prague, CZ-11000
35 Prague, Czech Republic

36 ^oUniversity of Warwick, Coventry CV4 7AL, United Kingdom

37 ^pBoston University, Boston, MA 02215, U.S.A.

38 ^qOsaka University, 1-1 Machikaney arna Toyonaka, Osaka 560-0043, Japan

39 ^rSaga University, Saga 840-8502, Japan

40 ^sLaboratoire Souterrain de Modane, F-73500 Modane, France

41 ^tFMFI, Comenius Univ., SK-842 48 Bratislava, Slovakia

42 ^uLSCE, CNRS, F-91190 Gif-sur-Yvette, France

43 ^vImperial College London, London SW7 2AZ, United Kingdom

44 ^wInstitut Universitaire de France, F-75005 Paris, France

45 ^xJyväskylä University, FIN-40351 Jyväskylä, Finland

46 ^yMHC, South Hadley, Massachusetts 01075, U.S.A.

47 ^zInstitute for Nuclear Research, 03028 Kyiv, Ukraine

48 ^{aa}Charles University in Prague, Faculty of Mathematics and Physics, CZ-12116 Prague, Czech
49 Republic

50 **Abstract**

51 The double-beta decay of ^{82}Se to the 0_1^+ excited state of ^{82}Kr has been studied with
52 the NEMO-3 detector using 0.93 kg of enriched ^{82}Se measured for 4.75 y, corresponding
53 to an exposure of 4.42 kg·y. A dedicated analysis to reconstruct the γ -rays has been
54 performed to search for events in the $2e2\gamma$ channel. No evidence of a $2\nu\beta\beta$ decay to the
55 0_1^+ state has been observed and a limit of $T_{1/2}^{2\nu}({}^{82}\text{Se}, 0_{gs}^+ \rightarrow 0_1^+) > 1.3 \times 10^{21}$ y at 90% CL
56 has been set. Concerning the $0\nu\beta\beta$ decay to the 0_1^+ state, a limit for this decay has
57 been obtained with $T_{1/2}^{0\nu}({}^{82}\text{Se}, 0_{gs}^+ \rightarrow 0_1^+) > 2.3 \times 10^{22}$ y at 90% CL, independently from
58 the $2\nu\beta\beta$ decay process. These results are obtained for the first time with a tracko-calor
59 detector, reconstructing every particle in the final state.

60 *Keywords:* Double beta decay; Neutrino; ^{82}Se ; Excited State

61 **1. Introduction**

62 The search for the neutrinoless double-beta decay ($0\nu\beta\beta$) is of major importance
63 in neutrino and particle physics. Its observation would prove the Majorana nature of
64 the neutrino and would be the first evidence for lepton number violation. Up to now,
65 no evidence of such a process has been found and the best half-life limits are in the
66 10^{24} - 10^{26} y range [1–4]. ^{82}Se is one of the best isotopes to investigate $0\nu\beta\beta$ decay. In
67 particular, its high $Q_{\beta\beta}$ -value of 2997.9 ± 0.3 keV [5] lies above the main backgrounds
68 coming from natural radioactivity. There exist also well-known methods of Se isotopic
69 enrichment through centrifugal separation. This is why ^{82}Se is the baseline isotope for
70 past, current or future experiments such as LUCIFER [6], CUPID-0 [7] and SuperNEMO
71 [8]. Several studies have been performed in the past to search for $0\nu\beta\beta$ decay of ^{82}Se to
72 the ground state of ^{82}Kr and recently new limits on the half-life have been obtained with
73 the NEMO-3 (2.5×10^{23} y [9]) and CUPID-0 experiments (3.5×10^{24} y [10]).

74 The double-beta decay with emission of two neutrinos ($2\nu\beta\beta$) is a second order elec-
75 troweak process in the Standard Model. It allows the experimental determination of
76 the Nuclear Matrix Elements (NME) for such processes and provides a robust test for
77 the different nuclear models. It could constrain the quenching factor of the axial-vector
78 coupling constant g_A and give the possibility to improve the quality of NME calculations
79 for $0\nu\beta\beta$ decay [11–14]. This process has been observed for 11 double-beta isotopes with
80 a range of measured half-lives between 10^{18} - 10^{24} y [15, 16]. For ^{82}Se , several experiments
81 have measured the $2\nu\beta\beta$ decay to the ground state with the most precise half-life value to
82 date of $9.39 \pm 0.17(\text{stat}) \pm 0.58(\text{syst}) \times 10^{19}$ y measured with the NEMO-3 experiment
83 [9].

84 The search for $\beta\beta$ decay to excited states is also an interesting way to study such
85 processes. Indeed, these decays have a very clear-cut signature using the $2e1\gamma$ channel (to

*Corresponding authors

Email addresses: fperrot@cenbg.in2p3.fr (F. Perrot), soule@cenbg.in2p3.fr (B. Soulé)

¹Deceased

86 the 2_1^+ state) or the $2e2\gamma$ channel (to the 0_1^+ or 2_2^+ state) which can dramatically reduce
 87 the number of background events. The disadvantages are a lower $Q_{\beta\beta}$ available energy for
 88 electrons which suppresses the probability of the decay and a lower detection efficiency
 89 for electrons and γ -rays. Nevertheless, the decay to excited states is of importance to test
 90 the nuclear matrix elements. A detailed analysis for $2\nu\beta\beta$ decay of ^{100}Mo and ^{150}Nd to
 91 the excited 0_1^+ state of ^{100}Ru and ^{150}Sm , respectively, showed that corresponding NME
 92 are only suppressed by $\sim 30\%$ when compared with the NME to ground state transition
 93 [17–23].

94 Up to now, the $2\nu\beta\beta$ decay to excited states has only been observed for two isotopes:
 95 ^{100}Mo and ^{150}Nd with typical half-lives of 10^{20} - 10^{21} y [24]. It is important to note
 96 that this decay has been observed only to the 0_1^+ excited state (with the emission of
 97 two γ -rays) which is favoured compared to the decay to the 2_1^+ or 2_2^+ excited states.
 98 These measurements have been performed using both High Purity Germanium (HPGe)
 99 detectors by measuring only the γ -rays in the cascade [18, 21, 22, 25–29] and “tracker-
 100 calorimeter” detectors such as NEMO-3 able to measure the energies of both electrons
 101 and γ -rays [19, 30]. For ^{82}Se , there is up to now no evidence for such a decay. Stringent
 102 limits have been obtained by the LUCIFER collaboration for the $(2\nu+0\nu)\beta\beta$ decay to
 103 various excited states of ^{82}Kr using a HPGe detector [31]. Nevertheless, this technique
 104 using only γ -rays does not allow to distinguish between $2\nu\beta\beta$ and $0\nu\beta\beta$. More recently,
 105 more stringent limits have been set by the CUPID-0 collaboration for the $0\nu\beta\beta$ decay to
 106 various excited states of ^{82}Kr using ZnSe scintillating bolometers [32].

107 In this work, we will present a detailed study of the ^{82}Se $2\nu\beta\beta$ and $0\nu\beta\beta$ decays to
 108 the 0_1^+ excited state of ^{82}Kr , expected to be the most favoured [33, 34], with the full
 109 exposure of the NEMO-3 experiment. In this analysis, we have access to the full topology
 110 of the decay. It consists of the emission of two electrons sharing 1510.2 keV of energy
 111 and accompanied by two γ -rays with energies of 711.2 keV and 776.5 keV respectively, as
 112 illustrated in Figure 1. After a presentation of the NEMO-3 detector, the ^{82}Se source foils
 113 and the associated backgrounds, we will present a dedicated analysis tool called gamma
 114 tracking (GT) developed to reconstruct efficiently the γ -rays in such a decay. Finally, we
 115 will present the results of the $2\nu\beta\beta$ and $0\nu\beta\beta$ decays of ^{82}Se to the 0_1^+ excited state of
 116 ^{82}Kr with the full NEMO-3 exposure of 4.42 kg.y.

117 2. NEMO-3 detector, ^{82}Se source foils and associated backgrounds

118 2.1. NEMO-3 detector

119 NEMO-3 was a detector installed in the Modane Underground Laboratory (LSM)
 120 under 4800 m water-equivalent in order to be protected against cosmic muons. It took
 121 data from February 2003 to January 2011. It consisted of a hollow cylinder divided
 122 into 20 sectors hosting thin source foils from 7 different enriched isotopes with a typical
 123 thickness of approximately 50 mg/cm² (as shown in Figure 2). The main isotope to
 124 search for $0\nu\beta\beta$ decay was ^{100}Mo with a total mass of 6.914 kg. The second isotope of
 125 interest was ^{82}Se with a mass of 0.932 kg shared in 3 sectors. The five other isotopes
 126 studied were by decreasing order of mass: ^{130}Te (0.454 kg), ^{116}Cd (0.405 kg), ^{150}Nd (36.55
 127 g), ^{96}Zr (9.43 g), and ^{48}Ca (6.99 g) (see [1, 35] for more details).

128 The source foils were hung at the center of a wire chamber composed of 6180 cells
 129 operating in Geiger mode. The gas was a mixture composed of 94.85% helium, 4%

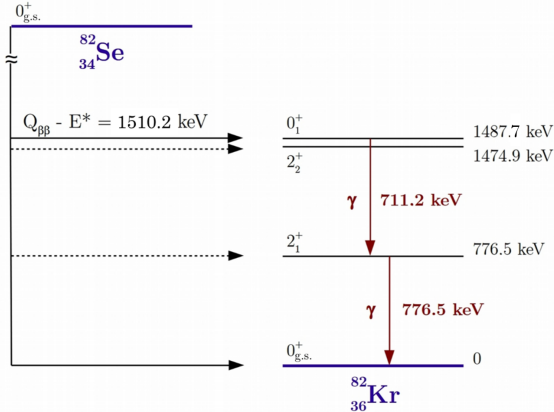


Figure 1: Decay scheme of the ^{82}Se $\beta\beta$ decay to the 0_1^+ excited state with the emission of two electrons sharing 1510.2 keV and two prompt γ -rays with energies of 711.2 and 776.5 keV [36].

130 ethanol, 1% argon and 0.15% of water vapour. These cells were placed inside a 25
 131 G magnetic field produced by a solenoid surrounding the detector. Charged particles
 132 thus had a curved trajectory when crossing the tracking chamber, which allowed the
 133 identification of a negative curvature for 95% of electrons at 1 MeV. The minimal distance
 134 traveled by a particle crossing the tracker is ~ 1.1 m, which corresponds to a typical
 135 minimal time of flight of ~ 3 ns. The resolution of the tracker was 0.5 mm transverse to
 136 the wires and 8 mm in the vertical direction for 1 MeV electrons.

137 A calorimeter enclosed the wire chamber. It was made from 1940 plastic scintillator
 138 blocks, each one with a typical size of $20 \times 20 \times 10 \text{ cm}^3$ and coupled to a low background
 139 photomultiplier (PMT) through a light guide. The calorimeter measured the kinetic
 140 energy of the particles and the time difference between two distant hits could be recorded.
 141 The blocks had an energy resolution of $6 - 7\% / \sqrt{E(\text{MeV})}$ and a time resolution of 250
 142 ps (σ at 1 MeV).

143 NEMO-3 was a unique detector as it combined tracking and calorimetry techniques.
 144 A charged particle (e^- , e^+ ...) was identified when going across and ionizing the wire
 145 chamber gas. Its track was associated to an energy deposit in a calorimeter block neigh-
 146 bouring the last fired Geiger cell. γ -rays were identified when energy was deposited in a
 147 calorimeter block but no track was associated. Alpha particles were identified as straight,
 148 short tracks as they could not travel more than ~ 40 cm in the tracker due to their high
 149 ionisation energy loss.

150 In order to run in low background conditions, the NEMO-3 detector had to be pro-
 151 tected from natural radioactivity. To do so, a passive shielding of 19 cm iron was sur-
 152 rounding the detector in order to stop external γ -rays. In addition, borated water,
 153 paraffin and wood were also used to moderate and absorb the environmental neutrons.
 154 For a more detailed description of the NEMO-3 detector, see [35].

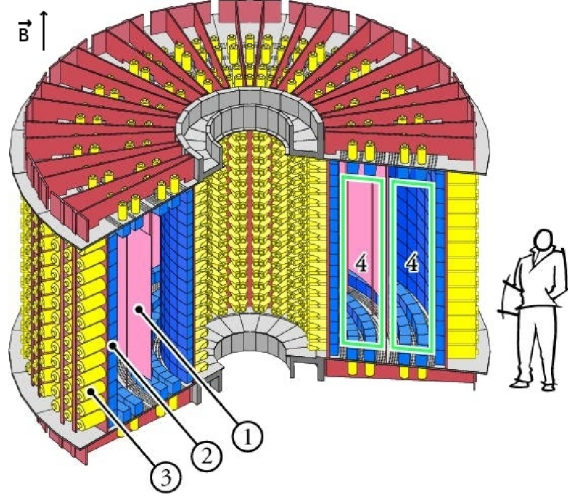


Figure 2: Cross-sectional view of the NEMO-3 detector. The detector consists of source foils (1), scintillators (2), photomultipliers (3) and a wire chamber (4).

155 2.2. ^{82}Se source

156 Two different batches of ^{82}Se source were used (referred to as $^{82}\text{Se}(\text{I})$ and $^{82}\text{Se}(\text{II})$).
 157 Those batches had an enrichment factor of $97.02 \pm 0.05\%$ and $96.82 \pm 0.05\%$ respectively.
 158 To produce source foils, the enriched ^{82}Se powder was mixed with polyvinyl alcohol
 159 (PVA) glue and deposited between $\sim 23 \mu\text{m}$ thick Mylar foils, producing composite source
 160 foils. The total mass of the ^{82}Se isotope in NEMO-3 was $932.4 \pm 5.0 \text{ g}$. An analysis of
 161 these ^{82}Se foils was conducted in order to search for $2\nu\beta\beta$ and $0\nu\beta\beta$ decays to ground
 162 state and is detailed in [9].

163 2.3. Backgrounds

164 With its powerful topology reconstruction ability, the NEMO-3 detector was able to
 165 identify $2e2\gamma$ events that were selected for $\beta\beta$ decay to excited states. However, some
 166 background isotopes could also produce this type of event. Among them, ^{214}Bi and ^{208}Tl
 167 decays were the main sources of background as the produced particles could carry similar
 168 energies as the β and γ particles from double beta decays to excited states. These two
 169 isotopes are β^- emitters from the ^{238}U and ^{232}Th radioactive decay chains, respectively,
 170 with Q -values of 3.27 and 4.99 MeV.

171 The main background contribution came from contamination in the source foils in-
 172 troduced during isotope production and residual contamination after isotope purification
 173 or during the foil production. This is described as *internal* contamination. In this case,
 174 those β emitting isotopes could produce two electrons coming from the same vertex via
 175 β -decay with internal conversion, β -decay followed by Møller scattering or β -decay to an
 176 excited state with a Compton scattering of the emitted photon. From these mechanisms,
 177 additional γ -rays could be produced by bremsstrahlung or from a decay to an excited
 178 state as presented in Figure 3. Prior to their installation, the activity of ^{82}Se foils in

179 ^{214}Bi and ^{208}Tl had been measured by low background gamma spectrometry using HPGe
 180 detectors. These small contaminations had been also measured and cross-checked by the
 181 NEMO-3 detector itself thanks to its capability to measure own background. In NEMO-
 182 3, the ^{214}Bi contamination of the foils could be studied by looking for the so called BiPo
 183 effect using ^{214}Bi and ^{214}Po sequential decay events. The β -decay of ^{214}Bi is followed by
 184 the α -decay of ^{214}Po with a half-life of $164.3 \mu\text{s}$. The analysis channel used to study such
 185 events was the $1e1\alpha(n)\gamma$ channel. ^{208}Tl decays exclusively to excited states and emits
 186 mostly 2 or 3 γ -rays (99.9%). Its contamination was thus measured through the $1e2\gamma$
 187 channel with a high γ -rays efficiency (about 50% at 1 MeV). Results and comparison of
 188 the ^{214}Bi and ^{208}Tl activities for ^{82}Se source foils using HPGe and NEMO-3 data are
 189 presented in Table 1 (including some other minor background isotopes [9]).

190 Finally, $2\nu\beta\beta$ decay to the ground state was also considered as a background source
 191 for $2\nu\beta\beta$ decay to excited states. When two electrons were produced, two extra γ -rays
 192 could be emitted via bremsstrahlung. A $2e2\gamma$ event was thus detected while excited
 193 states were not involved.

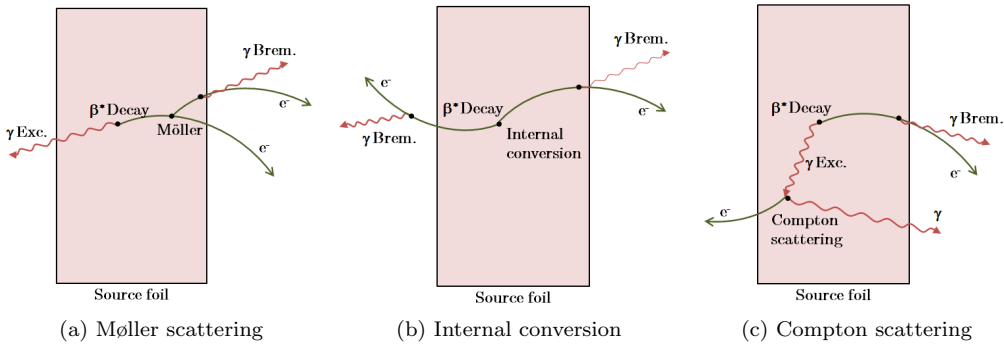


Figure 3: Mechanisms producing $2e2\gamma$ events from internal contamination of β emitters inside the source foils. β -decay to excited state followed by Møller scattering and bremsstrahlung (3(a)), β -decay to excited state with internal conversion and double bremsstrahlung (3(b)), β -decay to excited state followed by Compton scattering and bremsstrahlung (3(c)).

194 In addition to the *internal* contamination of the source foils, radioactivity from other
 195 components of the detector can produce background events, leading to γ -rays. These
 196 γ -rays then interact with the source foil and two electrons coming from the same vertex
 197 can then be reconstructed if there is either pair production with misreconstruction of
 198 the positron track, double Compton scattering or simple Compton scattering followed
 199 by Møller scattering of the produced electron. In the case of pair production, there can
 200 be annihilation of the positron which produces two photons. Considering that γ -ray
 201 interactions are involved in all those mechanisms, they have to be taken into account in
 202 the search of the $2\nu\beta\beta$ and $0\nu\beta\beta$ decay to the 0_1^+ excited state, with 2 γ -rays emitted
 203 in cascade. The different processes responsible for background production are described
 204 in Figure 4. The radioactivity of these external elements was first screened by low
 205 background γ -spectrometry. Also, when background isotopes produce a γ -ray, it can

Isotope	NEMO-3 (mBq/kg)	HPGe (mBq/kg)
^{214}Bi	1.62 ± 0.05	1.2 ± 0.5
^{208}Tl	0.39 ± 0.01	0.40 ± 0.13
$^{234\text{m}}\text{Pa}$	16.7 ± 0.1	< 18
^{40}K	58.9 ± 0.2	55 ± 5

Table 1: Results of the contamination measured in the ^{82}Se source foils by using independently NEMO-3 and HPGe data. All uncertainties are of statistical origin only, given at the 1σ level. The limit shown is at the 2σ level. The activities of ^{214}Bi and ^{208}Tl are derived from this independent analysis and are consistent with the ones already published in [9].

206 interact close to the surface of a calorimeter block and produce an electron. The latter
 207 crosses the whole wire chamber including the source foil. The initial γ -ray can also
 208 deposit energy in the calorimeter before interacting with the source and producing an
 209 electron. The contamination of external elements can thus be measured through two
 210 channels : crossing electron or (γ, e) external, i.e. Compton scattering in a scintillator
 211 block, producing a γ -ray energy deposit, followed by a Compton scattering in the source
 212 foil, emitting an electron detected in another scintillator block. An *external* background
 213 model was produced and can be found in [38].

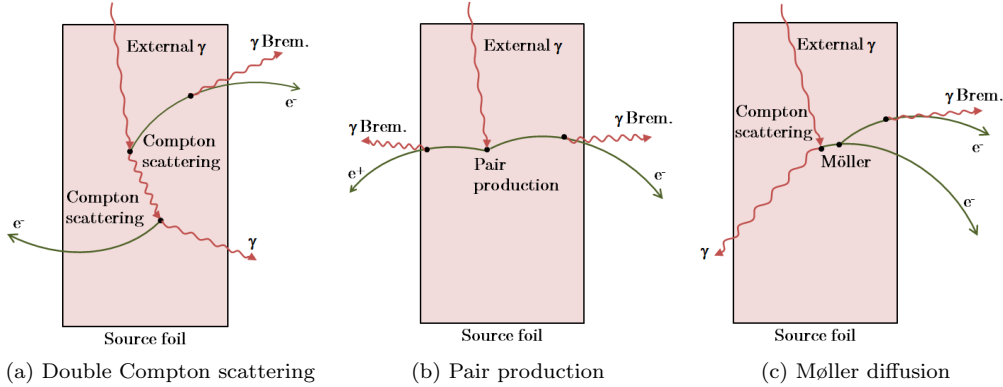


Figure 4: Mechanisms producing $2e2\gamma$ events from external contamination of the NEMO-3 detector emitting a γ -ray interacting inside the source foil. Double Compton scattering of the external γ -ray with bremsstrahlung in 4(a), pair production from the external γ -ray with double bremsstrahlung effects and poor reconstruction of the positron in 4(b), Compton scattering of the external γ -ray followed by a Møller scattering of the electron and a bremsstrahlung in 4(c).

214 A specific *external* background is the *radon* background. It comes from ^{222}Rn , a
 215 gaseous isotope in the ^{238}U chain. ^{222}Rn can be introduced via several mechanisms
 216 including emanation from detector materials, diffusion from laboratory air through de-

217 tector seals or contamination of the wire chamber gas. This is only possible because of
218 its long half-life of 3.82 days. Once inside the detector, mainly positive ions are produced
219 from the radon decays. Because of their charge, they can drift and be deposited on the
220 source foils or tracker wires. There, they decay into ^{214}Bi near the source material. This
221 contamination can then be observed through the $1e1\alpha(n)\gamma$ channel.

222 For the first 18 months of data-taking, there was a relatively high level of ^{222}Rn inside
223 the detector. To reduce it, an anti-radon tent was built around the detector reducing
224 the radon level inside the wire chamber volume by a factor ~ 6 [1]. The higher radon
225 activity data-taking period is referred to as Phase 1 and the lower activity period that
226 came after as Phase 2.

227 Both data and Monte Carlo simulations (MC) of signal and background are processed
228 by the same reconstruction algorithm. The DECAY0 event generator [39] is used for
229 generation of initial kinematics and particles are tracked through a detailed GEANT3
230 based detector simulation [40].

231 3. Gamma tracking technique

232 In most double-beta-decay experiments, a crucial aspect is to precisely measure the
233 energy of the particles. Using the unique combination of tracking and calorimetry,
234 NEMO-3 extracts other observables (angle between two electrons, track curvature, vertex
235 position...) allowing a good discrimination of background and signal events. In addition,
236 one of the most important features is the measurement of the time of flight of the particles
237 inside the detector.

238 When looking for double-beta decays, selecting events with two electrons from the
239 same vertex is not a strong enough criterion as seen in section 2.3. The time of flight
240 measurement thus allows to reject external events by testing two hypothesis : the event
241 has an *internal* or an *external* origin. This test is made possible in NEMO-3 by the
242 knowledge of the particle track length, energy, time of flight and the energy and time
243 resolution (σ_t) of the calorimeter. It can be conducted for charged particles for which
244 tracks are reconstructed but also for γ -rays coming from the same vertex.

245 Time of flight for electrons is thus an essential parameter when looking for double-
246 beta decay. The next section will describe its measurement in NEMO-3 before a new
247 method for measuring γ -ray time of flight is presented. The latter is crucial since a more
248 accurate description of events containing γ -rays and a higher sensitivity to these events
249 will improve the efficiency and precision in the search for decays to excited states.

250 3.1. Time of flight calculation

251 In order to construct an hypothesis on the time ordering of an event, some energy
252 must be deposited in at least two calorimeter blocks and one particle track or more
253 must be reconstructed inside the wire chamber. This track also has to be associated
254 to one of the calorimeter hits. The other calorimeter hit with no associated track is
255 identified as a γ -ray. Figure 5 illustrates an event sketch in NEMO-3 with an electron
256 (one reconstructed track with one calorimeter hit) and a γ -ray (only a calorimeter hit)
257 coming from the same vertex.

258 Before making any time of flight calculation for an event, two hypotheses must be
259 considered : *internal* or *external* origin. Theoretical times of flight between the vertex

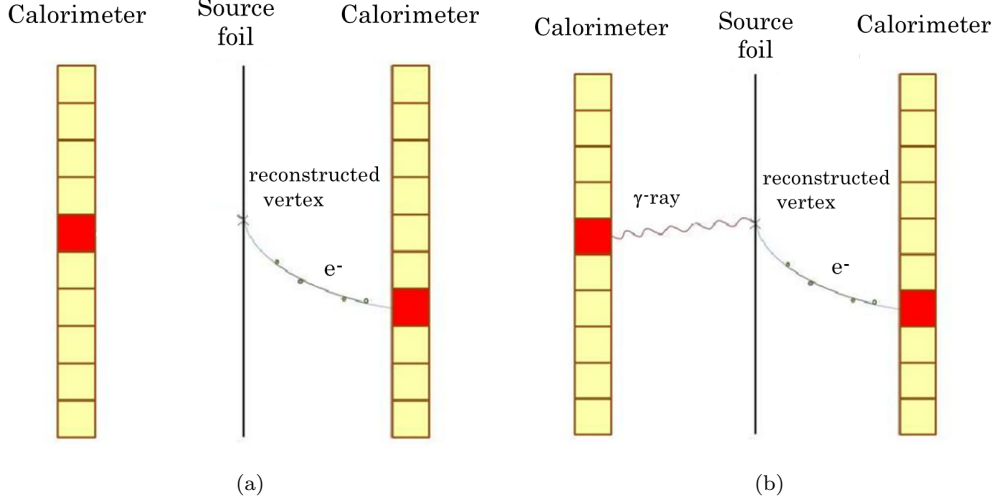


Figure 5: Event sketch with track reconstruction (5(a)) and scintillator association (5(b)). The reconstruction defines a γ -ray as energy deposit in a scintillator without any associated track. It can link it to the vertex in Figure 5(b).

260 and the calorimeter hit (t^{th}) that should be measured by the calorimeter (for each block
 261 hit) are then calculated for both hypotheses. The sum (*external* origin) or difference
 262 (*internal* origin) of these theoretical times is compared to the difference between times
 263 actually measured by the calorimeter (t^{exp}). If the given hypothesis is favoured, then the
 264 difference noted Δt_{hyp} must be close to zero, taking into account the time resolution of
 265 NEMO-3.

266 Considering the example presented in Figure 5(b), these differences for both hypothe-
 267 ses are expressed by the following equations :

$$\Delta t_{int} = (t_e^{th} - t_\gamma^{th}) - (t_e^{exp} - t_\gamma^{exp}) \quad (1)$$

$$\Delta t_{ext} = (t_e^{th} + t_\gamma^{th}) - (t_e^{exp} - t_\gamma^{exp}) \quad (2)$$

268 Nevertheless, the calculation of Δt_{hyp} is only a preliminary analysis. A more advanced
 269 study is based on the probability of time of flight and needs to take into account the
 270 uncertainties on theoretical and measured times. Thus the χ^2 method is used as described
 271 by :

$$\chi_{hyp}^2 = \frac{\Delta^2 t_{hyp}}{\sigma_{tot}^2}, \quad (3)$$

272 where σ_{tot}^2 is the quadratic sum of all uncertainties affecting time measurements or calcu-
 273 lations. These are the uncertainties on track lengths (for charged particles), path lengths
 274 (for γ -ray), measured energies (due to calorimeter energy resolution) and times (due to
 275 calorimeter time resolution).

276 When considering *external* or *internal* events, as in section 4, the selections will be
 277 based on the chi-squared probabilities for the respective hypotheses.

278 3.2. Gamma tracking

279 Another type of time of flight calculation is possible considering only the trajectory of
 280 photons. Because of the thickness of NEMO-3 scintillators, γ -rays do not always deposit
 281 all their energy inside a single block. One photon can deposit part of its energy in a
 282 calorimeter block after Compton scattering, then hit another one and potentially more.
 283 Gamma tracking is an original and powerful analysis tool developed recently [41] in order
 284 to take this effect into account and reconstruct the complete trajectory of γ -rays inside
 285 the detector, with each step from one scintillator to the next.

286 When a single γ -ray is produced inside a source foil with one or more charged particles
 287 and hits several scintillators, a few PMTs measure energies without associating them
 288 to reconstructed tracks. Figure 6(a) describes the approach presented in the previous
 289 section, where every unassociated hit is considered as having a different origin. Here,
 290 the second unassociated block is neither *internal* nor *external* and the event is excluded
 291 when selecting events for the $2e1\gamma$ channel. Using gamma tracking, the same event can
 292 be properly reconstructed as shown in Figure 6(b) : the second unassociated hit is paired
 293 with the first one under the assumption of Compton scattering and the event satisfies
 294 the $2e1\gamma$ channel conditions.

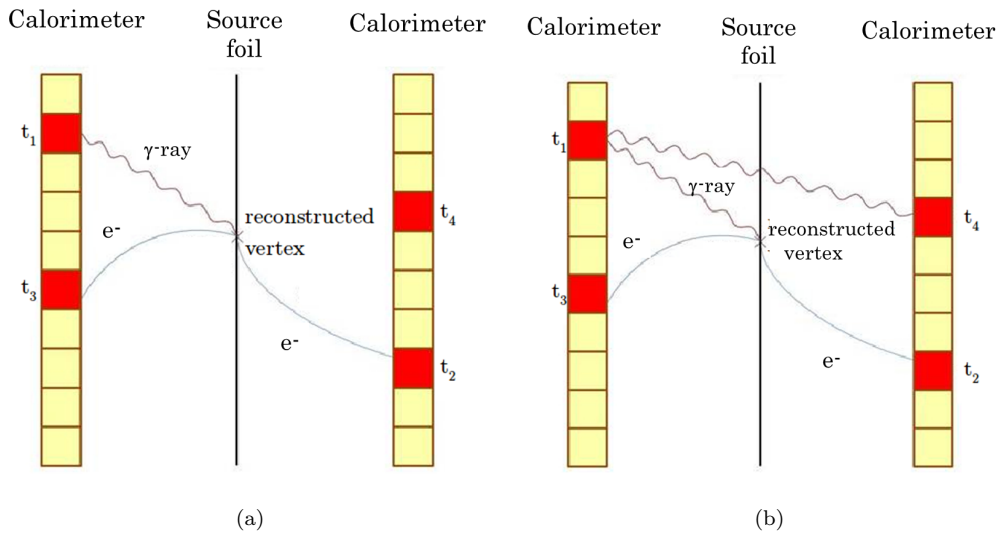


Figure 6: Example of an event reconstruction without using gamma tracking (6(a)). Only one of the two scintillators not associated to a track is consistent with the *internal* hypothesis, the other is neither *internal* nor *external*. The same event is reconstructed with gamma tracking (6(b)), the second scintillator can be associated to the first one under the assumption of Compton scattering.

295 In this example, the complete reconstruction of the photon can be done with only

296 one time of flight probability calculation : between the two scintillators not associated to
 297 any track. However, when events include several unassociated calorimeter blocks, every
 298 combination has to be taken into account and evaluated. In that case, before making
 299 a complete calculation, the probability of time of flight is determined for each pair of
 300 blocks in the event, with once again the χ^2 method. All the pairs are then combined to
 301 extract all possible topologies, each associated to a combined time of flight probability,
 302 using the equation :

$$\chi_{GT_{tot}}^2 = \sum_{n=1}^{n=m} \chi_{GT}^2(Block_{n-1}Block_n), \quad (4)$$

303 with m the total number of blocks involved in the chain of hit scintillator by a single
 304 γ -ray, $Block_{n-1}Block_n$ a pair of calorimeter blocks and $\chi_{GT}^2(Block_{n-1}Block_n)$ the χ^2
 305 value calculated for each pair. The main drawback of this method is the computation
 306 time. To limit this effect, two additional conditions are applied : requiring an energy
 307 threshold of 150 keV for the energy deposit in each calorimeter block and only taking
 308 into account the probabilities greater than 0.1% for any combination.

309 Once all calculations have been performed, the topology with the highest probability
 310 is considered the most likely. This combination defines the number of photons in the
 311 event and their trajectories. The gamma tracking technique is thus key to the study of
 312 double-beta decays to excited states.

313 3.3. Validation of gamma tracking using calibration sources

314 During the data taking phase of NEMO-3, several calibration runs using three point-
 315 like ^{232}U radioactive sources, labelled 1, 2 and 3, were conducted. Their activities were
 316 measured through γ -spectrometry (HPGe detectors) and are given in Table 2, column 2.
 317 These sources are especially well suited for gamma tracking studies since they decay to
 318 the ^{228}Th nucleus which belongs to the natural ^{232}Th radioactive decay chain. At the
 319 end of the chain, it produces a ^{208}Tl nucleus which is a β^- emitter producing at least
 320 two γ -rays : e.g. 2.615 and 0.583 MeV.

321 We measured the activities of the ^{232}U sources using NEMO-3 analysis with and
 322 without gamma tracking. We can then compare the results with the activities measured
 323 by HPGe detectors. The main objectives are to confirm that the use of the gamma
 324 tracking method improves the signal efficiency and reduces the systematics. Several
 325 criteria are defined to only select events involving one electron and two γ -rays ($1e2\gamma$) since
 326 99.8% of ^{208}Tl decays produce these three particles. Using Monte-Carlo simulations, the
 327 efficiency with gamma tracking is determined to be 1.16% for this topology (compared to
 328 0.92% without gamma tracking) while 53082 data events are selected for source 3 with an
 329 acquisition time of 107.6 hours. The same analysis without gamma tracking, conducted
 330 on the same data sample, selected only 38956 events. About 27% more events were
 331 thus selected using gamma tracking, proving that part of the events involving Compton
 332 scattering are recovered, thus improving the efficiency. Figure 7 illustrates the number
 333 of scintillator blocks hit by a single γ -ray according to the path reconstruction calculated
 334 with the gamma tracking method. A reasonable agreement is obtained between data
 335 from the ^{232}U radioactive sources and Monte-Carlo simulations.

336 Futhermore, the ^{232}U sources activities obtained with gamma tracking are presented
 337 in Table 2 where they are compared to activities obtained without the use of gamma

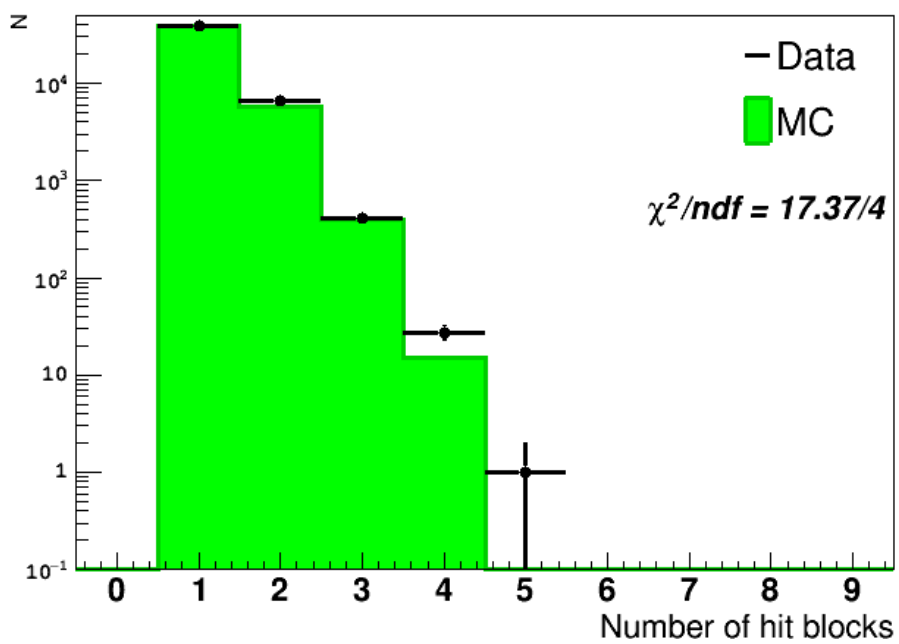


Figure 7: Number of scintillator blocks hit by a single γ -ray according to the path reconstruction calculated with the gamma tracking method, logarithmic scale. Data were acquired using γ -rays from the ^{232}U radioactive sources and are compared to Monte-Carlo simulations.

^{232}U	HPGe (Bq)	No GT act. (Bq)	Δ_{noGT} (%)	GT act. (Bq)	Δ_{GT} (%)
1	$7.79 \pm 0.04 \pm 0.21$	6.56 ± 0.08	15.8	6.98 ± 0.07	10.4
2	$15.91 \pm 0.09 \pm 0.43$	13.92 ± 0.13	12.5	14.88 ± 0.11	6.5
3	$32.76 \pm 0.17 \pm 0.89$	30.00 ± 0.17	8.4	32.11 ± 0.14	2.0

Table 2: Comparison of the ^{232}U sources activities measured by respectively γ -spectrometry (HPGe detector) and NEMO-3 analysis without and with the gamma tracking technique using the $1e2\gamma$ topology. Uncertainties in column 2 are respectively statistics and systematics. Columns 4 and 6 present the relative differences between HPGe and analysis activities (without and with gamma tracking).

tracking and to the γ -spectrometry measurements. The interaction of γ -rays may induce low energy deposits in the bulk of the scintillator block. The energy response of the calorimeter does not take into account the interaction point in the scintillator block so the effect of the energy threshold may be difficult to simulate. However, the main observation is that activities measured using gamma tracking are more consistent with the γ -spectrometry results.

However, activities measured through the analysis with gamma tracking are consistently lower than γ -spectrometry values. This difference is used as a way to estimate the systematic uncertainty induced by the use of the gamma tracking technique. The difference for sources 1, 2 and 3 are respectively 10.4%, 6.5% and 2.0% as reported in Table 2. As a conservative approach, the systematic uncertainty is considered to be 10%.

4. Double beta decay to the excited states

4.1. Two neutrino double-beta decay to 0_1^+ excited state

As mentioned in Section 1, $\beta\beta$ decays to the 0_1^+ excited state consist in the simultaneous emission (compared to the NEMO-3 time resolution) of two β and two γ particles. In order to select $2e2\gamma$ events, several criteria are applied to distinguish them from background events. The candidate events must contain two electron tracks, originating from the ^{82}Se source foil, each with an energy deposit greater than 150 keV. The distance between the tracks' intersections with the foil should fulfill Δ_{XY} less than 4 cm (perpendicular to the wires) and Δ_Z less than 8 cm (parallel to the wires) so they can be considered to have a common vertex. Two γ -rays must be reconstructed using the gamma tracking technique, each with a total energy greater than 150 keV. The timing of the calorimeter hits for electrons and γ -rays must be consistent with an *internal* event defined as those particles simultaneously emitted from their common vertex in the ^{82}Se foil. There should be no α -particle tracks and no extra reconstructed γ -rays in the event. 77 data events were selected from a total of 897,409,450 in the selenium sectors for the selected runs. Figure 8 shows that this number is compatible with the number of background events expected when using these criteria, as well as the energy distribution of both electrons for data events and background. Using these criteria, the efficiency for the expected signal is 0.078%.

These preselection criteria can be applied when looking for events including two internal electrons and γ -rays. In order to be more specific to the $2\nu\beta\beta(0_{gs}^+ \rightarrow 0_1^+)$ decay,

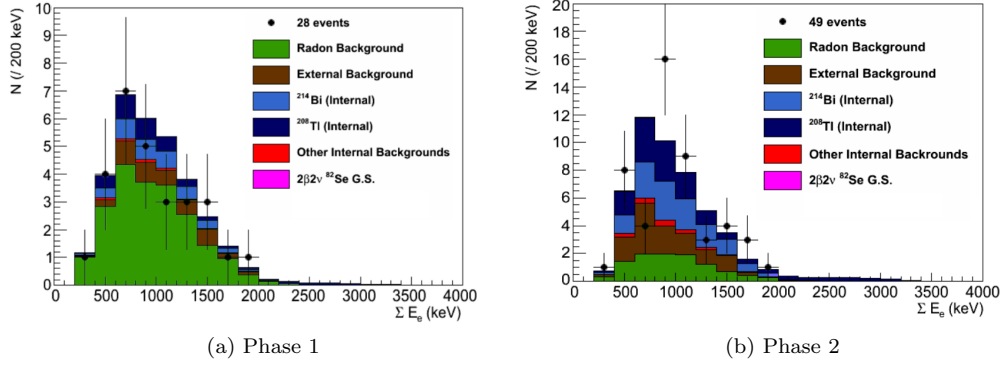


Figure 8: Sum of the electron energies distributions in the $2e2\gamma$ channel after the pre-selection criteria described in the text are applied, for Phase 1 in Figure 8(a) and Phase 2 in Figure 8(b). Data are compared to the MC prediction for the different backgrounds. The background coming from the $2\nu\beta\beta$ ^{82}Se decay to g.s. is completely negligible and thus not visible in the two plots.

370 an optimisation is made considering the energies of the four particles for this decay. The
 371 first energies to be optimized are the individual energies of both electrons labelled $E_{e \text{ min}}$
 372 and $E_{e \text{ max}}$. Both energies for each event are displayed using two-dimensional histograms
 373 for signal and total background, obtained from MC simulations as shown in Figures 9(a)
 374 and 9(b). For each bin of this two-dimensional histogram, the local statistical significance
 375 (noted N_{σ}^l) is calculated and displayed in Figure 9(c). This value is defined by
 376 the following equation :

$$N_{\sigma}^l = \frac{S^l}{\sqrt{S^l + B^l}}, \quad (5)$$

377 where S^l is the signal and B^l the background in each bin. The signal is given by the
 378 $2\nu\beta\beta$ to 0_1^+ state simulation with a half-life of 3×10^{20} years which is three times higher
 379 than the $2\nu\beta\beta$ decay to the ground state half-life.

380 The result of the optimization procedure was tested for several Monte Carlo samples,
 381 including $2\nu\beta\beta$ to the 0_1^+ state with various half-lives. If the half-life in the sample is
 382 different from 3×10^{20} y, the selection would not be optimal, thus the sensitivity to the
 383 $2\nu\beta\beta$ to the 0_1^+ excited state would be decreased. For samples with half-lives larger than
 384 3×10^{20} y, the optimization procedure gives a too loose selection w.r.t optimum, increas-
 385 ing the background contribution. For samples with half-lives smaller than 3×10^{20} y,
 386 the optimization procedure results in a too strict selection, reducing the signal efficiency.
 387 Even if not optimal, the selection would not bias the half-life of the sample.

388 A selection criterion is defined on N_{σ}^l for the maximised total statistical significance
 389 N_{σ} as presented in Figure 9(d). N_{σ} is calculated over the total number of simulated
 390 signal events and expected background.

391 In Figure 9(a), simulations show that the signal is stronger when the energies of

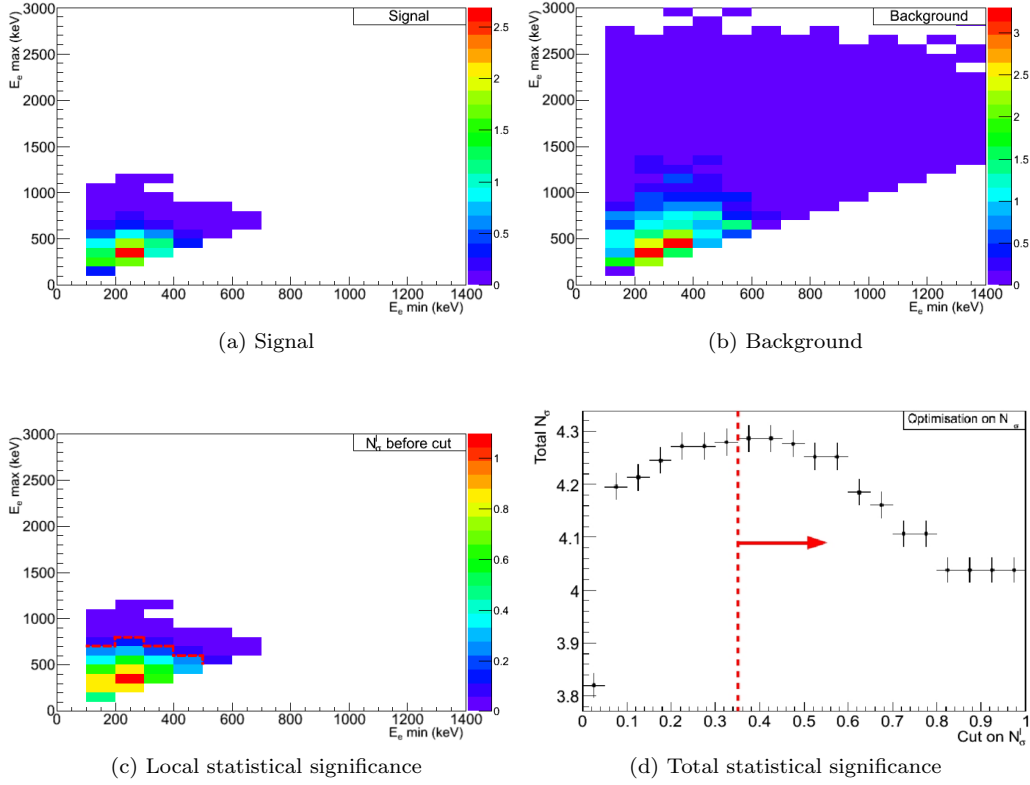


Figure 9: The distributions of signal $2\nu\beta\beta(0_{gs}^+ \rightarrow 0_1^+)$ and background events from MC simulation are represented in Figures 9(a) and 9(b) respectively, as a function of both electrons' individual energy. The local statistical significance N_σ^l distribution for the $2\nu\beta\beta(0_{gs}^+ \rightarrow 0_1^+)$ transition as a function of both electrons' individual energy is calculated for each bin of the 2-D histogram and represented in Figure 9(c). The total statistical significance N_σ as a function of a cut on the local significance in Figure 9(d) allows the optimization of this cut (dotted red line). Selected bins with high local statistical significance in Figure 9(c) are separated from the removed ones by the dotted red line.

392 the two electrons $E_{e \text{ max}}$ and $E_{e \text{ min}}$ are in the range of [300-400] and [200-300] keV,
393 respectively. This is due to their primary kinetic energies (with a total energy shared
394 equal or lower than 1510.2 keV) slightly affected by the loss of energy in the source foil
395 and in the tracking chamber. Concerning the background, the simulations in Figure 9(b)
396 show that the energies of the two detected electrons can be much higher, up to 2.7 MeV,
397 than those for the signal. This is due to the presence of ^{208}Tl isotope (Q -value of 4.99
398 MeV) which is one of the main backgrounds. Nevertheless, the optimization is able to
399 remove all the events with high energy electrons, typically greater than 1.1-1.2 MeV as
400 illustrated in Figure 9(c).

401 Other selections are then made on the total electron energy and total γ -rays energy
402 and finally on the two γ -rays' individual energies as seen respectively in Figures 10 and
403 11. Figure 10 shows some of the features of Figure 9, whereby the total energy of γ -
404 rays for background can be greater than 1500 keV due to higher energy γ -rays emitted in
405 ^{208}Tl decays (usually 2.61 and 0.58 MeV). The signal simulation fits the $2\nu\beta\beta(0_{gs}^+ \rightarrow 0_1^+)$
406 transition with the two electrons sharing 1512.2 keV and two γ -rays with a total energy
407 of 1487.7 keV. The optimisation process then only selects events with γ -rays sharing
408 less than 1600 keV, taking into account the energy resolution of the detector. Figure 11
409 represents the third step of optimization and concerns individual γ -rays energies. By this
410 stage, most of the ^{208}Tl induced events have been removed. Simulations indicate that
411 most of the remaining background events contain two γ -rays of [300-400] and [200-300]
412 keV. These can be related to ^{214}Bi , since its decay can produce a 609.3 keV γ -ray and
413 a lower energy one through bremsstrahlung, shown in Figure 3(a). Finally, most signal
414 events are expected to have two γ -rays of [400-500] and [500-600] keV, corresponding to
415 the $2\nu\beta\beta(0_{gs}^+ \rightarrow 0_1^+)$ γ -rays of 711.2 and 776.5 keV.

416 After the complete optimization process described here, the selection efficiency for
417 the $2\nu\beta\beta(0_{gs}^+ \rightarrow 0_1^+)$ signal calculated from MC is 0.069% with a total of 19 selected
418 data events.

419 The total electron energy distributions for Phase 1 and Phase 2 can be seen in Figure
420 12 while the total γ -rays energy distributions are shown in Figure 13. These figures also
421 show the different background contributions that are detailed in Table 3. The largest
422 contribution (52% in Phase 2) comes from internal contamination of the source foils and
423 especially from ^{214}Bi . Radon is also responsible for 68% of background events during
424 Phase 1 and was reduced to 28% in Phase 2. The external backgrounds account for 21%
425 of the total expected background despite the strong criteria used to ensure that only
426 internal events are selected.

427 It is also shown that there is a good compatibility with background and data events.
428 In the absence of a significant excess of data versus background, a limit has been set.
429 This can be performed using the following equation :

$$T_{1/2} > \epsilon \times N_{nuc} \times \ln(2) \times (t_{acq} - t_d) \times \frac{1}{N_{ex}}, \quad (6)$$

430 where ϵ is the detection efficiency, N_{nuc} the number of ^{82}Se nuclei, t_{acq} and t_d the
431 acquisition and dead time respectively and N_{ex} the number of signal events that can
432 be excluded. The method used here to obtain this last number is the CLs method [42],
433 that takes into account the shape of the expected signal and backgrounds as well as
434 the number of data events and several statistical and systematical uncertainties. The
435 systematics are detailed in Table 4. Considering then the 4.42 kg.y exposure, the 0.069%

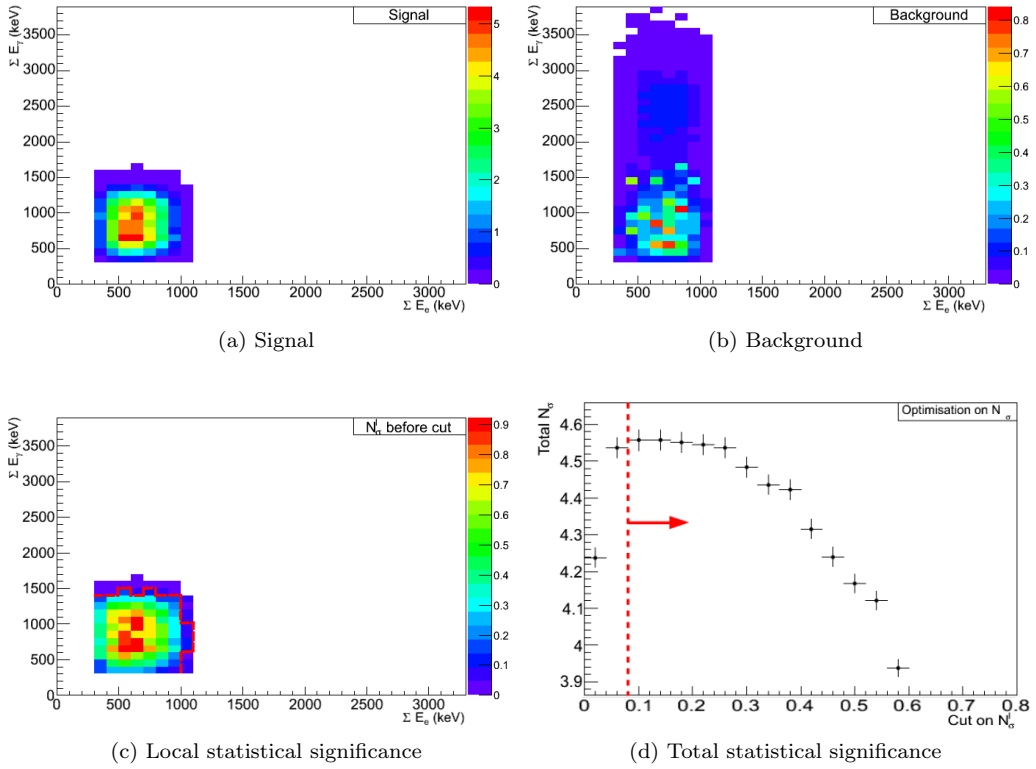


Figure 10: Total electron energy vs total γ -rays energy distributions for $2\nu\beta\beta(0_{gs}^+ \rightarrow 0_1^+)$ signal simulation (10(a)) and background (10(b)). Local statistical significance distributions for each bin of this histogram (10(c)) with optimisation cut (dotted red line) on total statistical significance N_σ presented in Figure 10(d).

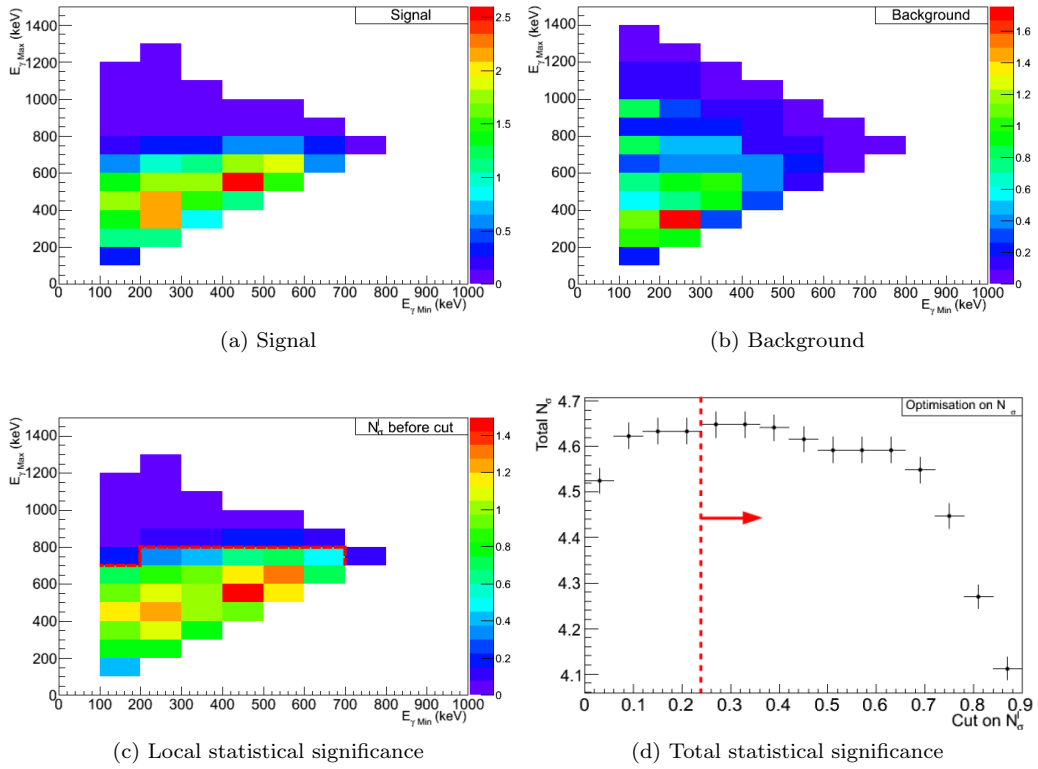


Figure 11: γ -ray 1 energy vs γ -ray 2 energy distributions for $2\nu\beta\beta$ ($0_{gs}^+ \rightarrow 0_1^+$) signal simulation (11(a)) and background (11(b)). Local statistical significance distributions for each bin of this histogram (11(c)) with optimisation cut (dotted red line) on total statistical significance N_{σ} presented in Figure 11(d).

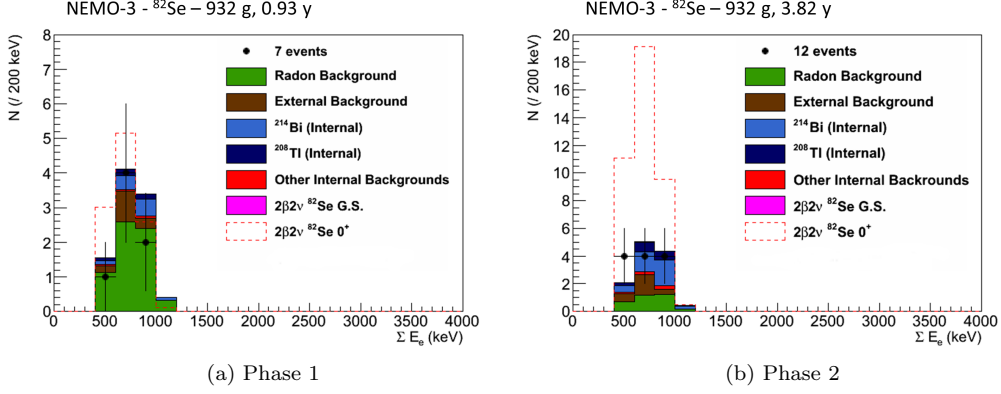


Figure 12: Total electron energy distributions after selection for the $2\nu\beta\beta(0_{gs}^+ \rightarrow 0_1^+)$ transition, for Phase 1 in Figure 12(a) and Phase 2 in Figure 12(b). Experimental data events are compared to the MC simulation for the different backgrounds. The dotted red line represents the simulated signal for a half-life of 3×10^{20} years.

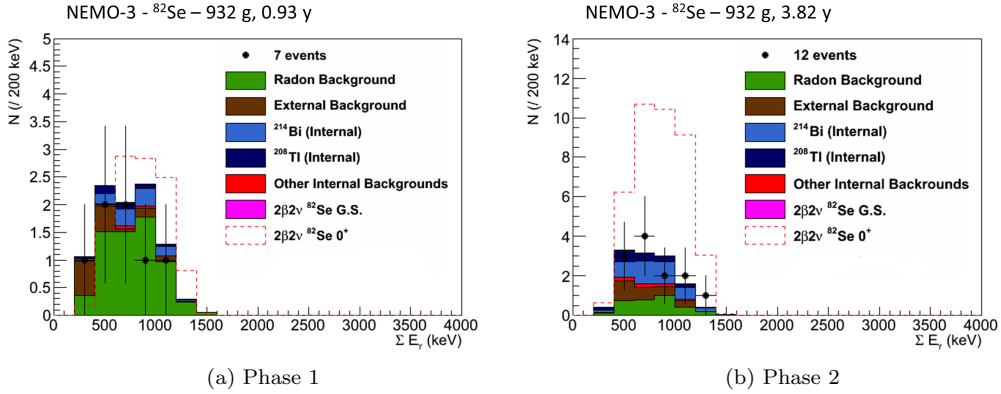


Figure 13: Total γ -rays energy distributions after selection for the $2\nu\beta\beta(0_{gs}^+ \rightarrow 0_1^+)$ transition, for Phase 1 in Figure 13(a) and Phase 2 in Figure 13(b). Experimental data events are compared to the MC simulation for the different backgrounds. The dotted red line represents the simulated signal with a half-life of 3×10^{20} years.

		Expected events		Contribution to total background (%)	
		Phase 1	Phase 2	Phase 1	Phase 2
Internal	^{214}Bi	$1.14 \pm 0.05 \pm 0.12$	$4.28 \pm 0.09 \pm 0.43$	12.1	36.1
	^{208}Tl	$0.43 \pm 0.02 \pm 0.07$	$1.58 \pm 0.04 \pm 0.23$	4.6	13.3
	Others	$0.06 \pm 0.03 \pm 0.01$	$0.29 \pm 0.14 \pm 0.02$	0.6	2.4
	Total	$1.64 \pm 0.07 \pm 0.20$	$6.15 \pm 0.49 \pm 0.68$	17.3	51.8
Radon		$6.44 \pm 0.63 \pm 0.65$	$3.26 \pm 0.31 \pm 0.33$	68.0	27.5
External	^{214}Bi	$0.38 \pm 0.19 \pm 0.04$	$1.49 \pm 0.75 \pm 0.15$	4.0	12.5
	^{208}Tl	$0.29 \pm 0.10 \pm 0.03$	$0.18 \pm 0.06 \pm 0.02$	2.9	1.6
	Others	$0.74 \pm 0.37 \pm 0.08$	$0.78 \pm 0.39 \pm 0.08$	7.8	6.6
	Total	$1.39 \pm 0.43 \pm 0.15$	$2.46 \pm 0.05 \pm 0.85$	14.7	20.7
Total background		$9.47 \pm 0.77 \pm 1.00$	$11.87 \pm 1.17 \pm 1.26$	100.0	100.0
Data events		7	12	–	–

Table 3: Numbers of expected background events from the main background sources in both Phases and their contribution to the total number of expected background events for the $2e2\gamma$ channel after optimisation for the study of $2\nu\beta\beta(0_{gs}^+ \rightarrow 0_1^+)$ decay. 0.93 year of data taking are considered for Phase 1 and 3.82 years for Phase 2. The quoted uncertainties represent the statistical and systematic uncertainties, respectively. The number of selected data events for each phase is also presented.

436 efficiency, the 21.4 expected background events and 19 data events, the limit on the $2\nu\beta\beta$
437 ($0_{gs}^+ \rightarrow 0_1^+$) decay half-life for ^{82}Se is, at 90% CL :

$$T_{1/2}^{2\nu}(^{82}\text{Se}, 0_{gs}^+ \rightarrow 0_1^+) > 1.3 \times 10^{21} \text{ y.} \quad (7)$$

438 This result is compatible with limit of 3×10^{21} y from Ref. [37] and lower than the
439 value published by the LUCIFER collaboration, who determined a limit of 3.4×10^{22} y
440 [31] for the $(2\nu+0\nu)\beta\beta$ processes. However, the NEMO-3 technique precisely identifies
441 the event topology and could thus independently study $2\nu\beta\beta$ and $0\nu\beta\beta$ processes.

442 4.2. Neutrinoless double beta decay to 0_1^+ excited state

443 The search for $0\nu\beta\beta$ events is carried out similarly to what has been done for the
444 $2\nu\beta\beta$ decay. The preselection criteria are the same as what is described in the first part
445 of Section 4.1. However, in the $0\nu\beta\beta$ process through the $0_{gs}^+ \rightarrow 0_1^+$ transition, the two
446 electrons do not share energy with neutrinos contrary to the $2\nu\beta\beta$ decay. The signal
447 efficiency using these criteria increases by a factor 10 compared to the $2\nu\beta\beta$ process.
448 It reaches 0.71%, as higher energy electrons are expected. The selection has then been
449 optimized with these energies, taking into account a simulated signal with a half-life of
450 3×10^{21} years and using the same method as the one described in Section 4.1. Applying
451 those criteria, the final selection efficiency for this signal is 0.69% and 14 data events are
452 selected.

453 The total electron energy distributions for Phase 1 and Phase 2 are shown in Figure
454 14. The background composition is similar to what was presented in Table 3 with a

Systematic	Estimated uncertainty (%)	Method of estimate
Gamma tracking	10.4	^{232}U vs HPGe
Energy calibration	1	Neutron sources
$2\nu\beta\beta$ efficiency	5	^{207}Bi vs HPGe
^{82}Se mass	0.5	Uncertainty on mass and enrichment
Energy loss in foil	1	Neutron sources
bremsstrahlung	1	^{90}Y source analysis
Ext. BG activities	10	Variation from background model
Radon BG activities	10	1e1 α vs 1e1 γ
Int. BG activities (excl. ^{208}Tl & ^{214}Bi)	4	^{207}Bi 1eN γ vs 2e (^{40}K & $^{234\text{m}}\text{Pa}$ meas. in 1e)
Int. ^{214}Bi activity	10	1e1 α vs. 1e1 γ
Int. ^{208}Tl activity	15	NEMO-3 vs HPGe
$2\nu\beta\beta$ activity	1	Statistical uncertainty

Table 4: Values of the 1σ systematic uncertainties included in the calculation of the limits on $2\nu\beta\beta$ decay to excited states and their methods of estimate. The estimated uncertainties come from the comparison of the activity measurements of calibration sources between NEMO-3 and HPGe (^{232}U , ^{207}Bi , ^{90}Y), the uncertainties on background measurements and uncertainties specific to the detector or ^{82}Se sources.

455 high radon contribution. The details are presented in Table 5. The total γ -rays energy
456 distributions are shown in Figure 15.

457 As for the $2\nu\beta\beta(0_{gs}^+ \rightarrow 0_1^+)$ transition, data is consistent with background-only pre-
458 dictions so a limit has to be set on the half-life of the $0\nu\beta\beta(0_{gs}^+ \rightarrow 0_1^+)$ process. The
459 method used to calculate such a limit remains the CLs method. With the 20.1 back-
460 ground events and the statistical and systematic uncertainties, the limit on the $0\nu\beta\beta$
461 ($0_{gs}^+ \rightarrow 0_1^+$) decay half-life for ^{82}Se (at 90% CL) is :

$$T_{1/2}^{0\nu}(^{82}\text{Se}, 0_{gs}^+ \rightarrow 0_1^+) > 2.3 \times 10^{22} \text{ y.} \quad (8)$$

462 This result is given for the $0\nu\beta\beta(0_{gs}^+ \rightarrow 0_1^+)$ transition for ^{82}Se , separately from
463 $2\nu\beta\beta(0_{gs}^+ \rightarrow 0_1^+)$. It is compatible with limit of 3.4×10^{22} y and 8.1×10^{22} y obtained in the
464 LUCIFER experiment [31] for the $(2\nu+0\nu)\beta\beta$ processes and CUPID-0 [32] experiment.
465 According to the mass mechanism, a Majorana neutrino is exchanged during such a
466 process and therefore a limit can also be set on the effective mass of the neutrino using
467 the following equation :

$$\frac{1}{\left(T_{1/2}^{0\nu}\right)_{MM}} = G^{0\nu}(Q_{\beta\beta}, Z) g_A^4 |M^{0\nu}|^2 \left| \frac{m_{\beta\beta}}{m_e} \right|^2, \quad (9)$$

468 where $G^{0\nu}(Q_{\beta\beta}, Z)$ is the phase space factor given in [43] for the transition, $g_A = 1.27$
469 and $M^{0\nu}$ the nuclear matrix element [12, 13, 44, 45]. The limit that can be set on the
470 effective neutrino mass is $m_{\beta\beta} < [42 - 239]$ eV.

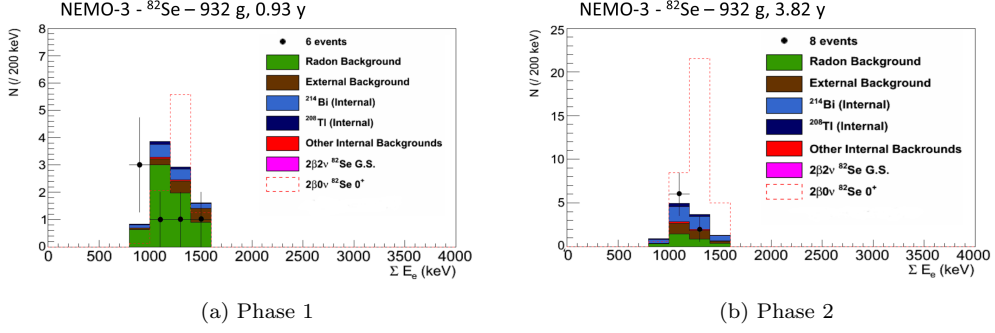


Figure 14: Total electron energy distributions after selection for the $0\nu\beta\beta$ ($0_{gs}^+ \rightarrow 0_1^+$) transition, for Phase 1 in Figure 14(a) and Phase 2 in Figure 14(b). Experimental data events are compared to the MC simulation for the different backgrounds. The dotted red line represents the simulated signal with a half-life of 3×10^{21} years.

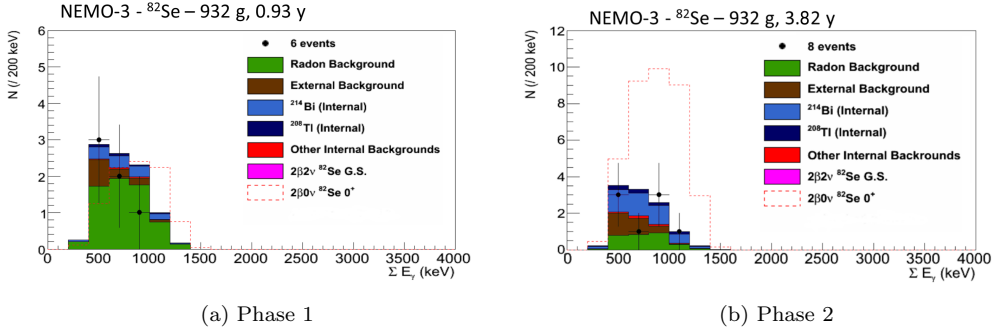


Figure 15: Total γ -rays energy distributions after selection for the $0\nu\beta\beta$ ($0_{gs}^+ \rightarrow 0_1^+$) transition, for Phase 1 in Figure 15(a) and Phase 2 in Figure 15(b). Experimental data events are compared to the MC simulation for the different backgrounds. The dotted red line represents the simulated signal with a half-life of 3×10^{21} years.

		Expected events		Contribution to total background (%)	
		Phase 1	Phase 2	Phase 1	Phase 2
^{82}Se foils	^{214}Bi	$1.25 \pm 0.05 \pm 0.13$	$4.57 \pm 0.10 \pm 0.46$	13.5	41.9
	^{208}Tl	$0.24 \pm 0.01 \pm 0.03$	$0.82 \pm 0.02 \pm 0.12$	2.6	7.6
	Others	$0.02 \pm 0.01 \pm 0.01$	$0.07 \pm 0.03 \pm 0.01$	0.2	0.6
	Total	$1.50 \pm 0.06 \pm 0.17$	$5.46 \pm 0.11 \pm 0.59$	16.3	50.1
Radon		$6.50 \pm 0.64 \pm 0.65$	$2.97 \pm 0.27 \pm 0.30$	70.4	27.3
Detector	^{214}Bi	$0.45 \pm 0.22 \pm 0.05$	$1.33 \pm 0.62 \pm 0.14$	4.9	12.3
	^{208}Tl	$0.79 \pm 0.09 \pm 0.08$	$1.13 \pm 0.14 \pm 0.12$	8.5	10.3
	Others	0	0	0	0
	Total	$1.24 \pm 0.24 \pm 0.13$	$2.46 \pm 0.62 \pm 0.26$	13.4	22.6
Total background		$9.24 \pm 0.69 \pm 0.95$	$10.89 \pm 0.69 \pm 1.15$	100.0	100.0
Data events		6	9	–	–

Table 5: Numbers of expected background events from the main background sources in both Phases and their contribution to the total number of expected background events for the $2e2\gamma$ channel after optimisation for the study of $0\nu\beta\beta(0_1^+ \rightarrow 0_2^+)$ decay. 0.93 years of data taking are considered for Phase 1 and 3.82 years for Phase 2. The quoted uncertainties represent the statistical and systematic uncertainties, respectively. The number of selected data events for each phase is also presented.

471 5. Summary and Conclusions

472 4 Using an innovative gamma tracking technique, the NEMO-3 data set was analysed
473 to search for $\beta\beta$ decays of ^{82}Se to the excited states of ^{82}Kr with a 4.42 kg.y exposure. No
474 evidence for the $2\nu\beta\beta$ process was found and thus an upper limit on the decay half-life
475 was set at 90% CL : $T_{1/2}^{2\nu}(^{82}\text{Se}, 0_{gs}^+ \rightarrow 0_1^+) > 1.3 \times 10^{21}$ y. This result can nevertheless
476 help to constrain theoretical QRPA models presented in [33, 34, 46].

477 The analysis of the $0\nu\beta\beta$ decay to excited states was conducted in a similar fashion
478 and, as once again no extra events were observed over the expected background, an upper
479 limit was set at 90% CL : $T_{1/2}^{0\nu}(^{82}\text{Se}, 0_{gs}^+ \rightarrow 0_1^+) > 2.3 \times 10^{22}$ y. These results are obtained
480 for the first time with a detector which reconstructs each particle individually in the final
481 state.

482 This analysis performed with ^{82}Se in NEMO-3 will also provide useful information
483 for the next-generation SuperNEMO experiment which will host 100 kg of ^{82}Se , such as
484 optimisation of the selected events and identification of the main background contribu-
485 tions.

486 In parallel with its search for $0\nu\beta\beta$ decay to the ground state, SuperNEMO will also
487 look for the $2\nu\beta\beta$ and $0\nu\beta\beta$ decays to excited states with major improvements. Using
488 thicker scintillators, the sensitivity to γ -rays and efficiency to $2\nu\beta\beta$ and $0\nu\beta\beta(0_{gs}^+ \rightarrow 0_1^+)$
489 transitions will be enhanced. Backgrounds will also be reduced : more than a factor 30 for
490 radon and a factor 100 for ^{214}Bi and ^{208}Tl . The expected sensitivities for SuperNEMO
491 are respectively $\sim 10^{23}$ y and $\sim 10^{24}$ y for the $2\nu\beta\beta$ and $0\nu\beta\beta(0_{gs}^+ \rightarrow 0_1^+)$ half-lives.
492 A first module, called Demonstrator, with 7 kg of ^{82}Se is undergoing commissioning

493 and will start taking data in 2019. Its goal is to reach a sensitivity on the $0\nu\beta\beta$ half-
494 life of 5×10^{24} y in 17.5 kg·y exposure with the demonstration of a “zero”-background
495 experiment [47].

496 **Acknowledgements** We thank the staff of the Modane Underground Laboratory
497 for their technical assistance in running the experiment. We acknowledge support by the
498 grants agencies of the Czech Republic (grant number EF16 013/0001733), CNRS/IN2P3
499 in France, RFBR in Russia (Project No.19-52-16002 NCNIL a), APVV in Slovakia
500 (Project No. 15-0576), STFC in the UK and NSF in the USA.

501 References

- 502 [1] R. Arnold et al. (NEMO-3 Collaboration) (NEMO-3 Collaboration), Phys. Rev. D **92** (2015)
503 072011. URL: <https://link.aps.org/doi/10.1103/PhysRevD.92.072011>. doi:10.1103/PhysRevD.
504 92.072011.
- 505 [2] C. Alduino et al. (CUORE Collaboration) (CUORE Collaboration), Phys. Rev. Lett. **120**
506 (2018) 132501. URL: <https://link.aps.org/doi/10.1103/PhysRevLett.120.132501>. doi:10.1103/
507 PhysRevLett.120.132501.
- 508 [3] M. Agostini et al. (GERDA Collaboration) (GERDA Collaboration), Phys. Rev. Lett. **120**
509 (2018) 132503. URL: <https://link.aps.org/doi/10.1103/PhysRevLett.120.132503>. doi:10.1103/
510 PhysRevLett.120.132503.
- 511 [4] A. Gando et al. (KamLAND-Zen Collaboration) (KamLAND-Zen Collaboration), Phys. Rev. Lett.
512 **117** (2016) 082503. URL: <https://link.aps.org/doi/10.1103/PhysRevLett.117.082503>. doi:10.
513 1103/PhysRevLett.117.082503.
- 514 [5] D. L. Lincoln et al., Phys. Rev. Lett. **110** (2013) 012501.
- 515 [6] J. W. Beeman et al. (LUCIFER Collaboration), Adv. High Energy Phys. **2013** (2013) 237973.
- 516 [7] O. Azzolini, et al., Eur. Phys. J. C **78** (2018) 428
- 517 [8] R. Arnold et al., Eur. Phys. J. C **70** (2010) 927–943.
- 518 [9] R. Arnold, et al. (NEMO-3 Collaboration), Eur. Phys. J. C **78** (2018) 821.
- 519 [10] O. Azzolini, et al., Phys. Rev. Lett. **123** (2019) 032501 doi:10.3390/PhysRevLett.123.032501.
- 520 [11] J. Menéndez, A. Poves, E. Caurier, F. Nowacki, Nuclear Physics A **818** (2009) 139–151.
521 URL: <http://www.sciencedirect.com/science/article/pii/S0375947408008233>. doi:[http://dx.
522 doi.org/10.1016/j.nuclphysa.2008.12.005](http://dx.doi.org/10.1016/j.nuclphysa.2008.12.005).
- 523 [12] J. Barea, J. Kotila, F. Iachello, Phys. Rev. C **91** (2015) 034304. URL: [https://link.aps.org/doi/
524 10.1103/PhysRevC.91.034304](https://link.aps.org/doi/10.1103/PhysRevC.91.034304). doi:10.1103/PhysRevC.91.034304.
- 525 [13] J. Hyvärinen, J. Suhonen, Phys. Rev. C **93** (2016) 064306. URL: [https://link.aps.org/doi/10.
526 1103/PhysRevC.93.064306](https://link.aps.org/doi/10.1103/PhysRevC.93.064306). doi:10.1103/PhysRevC.93.064306.
- 527 [14] M. J. Dolinski et al, Annu. Rev. Nucl. Part. Sci. **69** (2019) 219–251. URL: [https:
528 //www.annualreviews.org/doi/10.1146/annurev-nucl-101918-023407](https://www.annualreviews.org/doi/10.1146/annurev-nucl-101918-023407). doi:10.1146/
529 annurev-nucl-101918-023407.
- 530 [15] A. S. Barabash, Nucl. Phys. A **393** (2015) 593. URL: [https://www.sciencedirect.com/science/
531 article/pii/S037594741500010X?via%3Dihub](https://www.sciencedirect.com/science/article/pii/S037594741500010X?via%3Dihub). doi:10.1016/j.nuclphysa.2015.01.001.
- 532 [16] A. S. Barabash, [arXiv:nucl-ex/1907.06887](https://arxiv.org/abs/1907.06887).
- 533 [17] R. Arnold et al. (NEMO-3 Collaboration), Phys. Rev. Lett. **95** (2005) 182302. URL: [https://link.
534 aps.org/doi/10.1103/PhysRevLett.120.132501](https://link.aps.org/doi/10.1103/PhysRevLett.120.132501). doi:10.1103/PhysRevLett.120.132501.
- 535 [18] R. Arnold et al., Nucl. Phys. A **925** (2014) 25–36.
- 536 [19] R. Arnold et al., Nucl. Phys. A **781** (2007) 209–226.
- 537 [20] R. Arnold, et al. (NEMO-3 Collaboration), Phys. Rev. D **94** (2016) 072003. [https://link.aps.
538 org/doi/10.1103/PhysRevD.94.072003](https://link.aps.org/doi/10.1103/PhysRevD.94.072003). doi:10.1103/PhysRevD.94.072003.
- 539 [21] A. S. Barabash, Ph. Hubert, A. Nachab and V. I. Umatov, Phys. Rev. C **79** (2009) 45501.
- 540 [22] M. F. Kidd, J. H. Esterline, S. W. Finch and W. Tornow, Phys. Rev. C **90** (2014) 055501.
- 541 [23] J. Kotila, F. Iachello, Phys. Rev. C **85** (2012) 034316.
- 542 [24] A. S. Barabash, AIP Conf. Proc. **1894** (2017) 020002.
- 543 [25] A. S. Barabash, Phys. Lett. B **345** (1995) 408–413.
- 544 [26] A. S. Barabash, Phys. At. Nucl. **62** (1999) 2039–2043.
- 545 [27] L. De Braeckeeler, M. Hornish, A. S. Barabash, V. Umatov, Phys. Rev. Lett. **86** (2001) 3510–3513.
- 546 [28] M. F. Kidd et al, Nucl. Phys. A **821** (2009) 251–261.

- 547 [29] P. Belli et al, Nucl. Phys. A **846** (2010) 143–156.
- 548 [30] S. Blondel, Optimisation du blindage contre les neutrons pour le démonstrateur de SuperNEMO et
549 analyse de la double désintégration β du néodyme-150 vers les états excités du samarium-150 avec
550 le détecteur NEMO 3, PhD thesis, Université Paris Sud, 2013.
- 551 [31] J. W. Beeman et al. (LUCIFER Collaboration), Eur. Phys. J. C **75** (2015) 591.
- 552 [32] O. Azzolini et al. (CUPID-0 Collaboration), Eur. Phys. J. C **78** (2018) 888.
- 553 [33] M. Aunola, J. Suhonen, Nucl. Phys. A **602** (1996) 133–166.
- 554 [34] J. Suhonen, O. Civitarese, Phys. Rep. **300** (1998) 123–214.
- 555 [35] R. Arnold, C. Augier, A. Bakalyarov, J. Baker, A. Barabash, et al., Nucl. Instrum. Meth. **A 536**
556 (2005) 79–122. doi:10.1016/j.nima.2004.07.194. arXiv:physics/0402115.
- 557 [36] J. K. Tuli, E. Brown, Nucl. Data Sheets, **157**, 260, 2019.
- 558 [37] J. Suhonen, J. Toivanen, A. S. Barabash, I. A. Vanushin, V. I. Umatov, R. Gurriarán, F. Hubert,
559 P. Hubert, Zeitschrift für Physik A Hadrons and Nuclei **358** (1997) 297–301. URL: <http://dx.doi.org/10.1007/s002180050333>. doi:10.1007/s002180050333.
- 560 [38] J. Argyriades, et al. (NEMO-3 Collaboration), Nucl. Instrum. Meth. **A 606** (2009) 449–465. doi:10.
561 1016/j.nima.2009.04.011. arXiv:0903.2277.
- 562 [39] O. Ponkratenko, V. Tretyak, Y. Zdesenko, Phys. Atom. Nucl. **63** (2000) 1282.
- 563 [40] R. Brun, F. Bruyant, M. Maire, A. McPherson, P. Zanarini CERNDD-EE-84-1 (1987) .
- 564 [41] C. Hugon, Analyse des données de l’expérience NEMO3 pour la recherche de la désintégration double
565 bêta sans émission de neutrinos. Étude des biais systématiques du calorimètre et développement
566 d’outils d’analyse, PhD thesis, Université Paris Sud, 2012.
- 567 [42] T. Junk, Nucl. Instrum. Meth. **A 434** (1999) 435–443. doi:10.1016/S0168-9002(99)00498-2.
568 arXiv:hep-ex/9902006.
- 569 [43] M. Mirea, T. Pahomi, S. Stoica, Rom. Rep. Phys. **67** (2015) 872–889.
- 570 [44] F. Šimkovic, M. Nowak, W. A. Kamiński, A. A. Raduta and A. Faessler Phys. Rev. C **64** (2001)
571 035501.
- 572 [45] J. Menéndez, A. Poves, E. Caurier, F. Nowacki, Nucl. Phys. A **818** (2009) 139–151.
- 573 [46] J. Toivanen, J. Suhonen, Phys. Rev. C **55** (1997) 2314–2323.
- 574 [47] F. Perrot (on behalf of the SuperNEMO collaboration), POS (ICHEP 2016) (2016) 499.
- 575